Rapid image stitching and computer-aided detection for multipass automated breast ultrasound

Ruey-Feng Chang
Department of Computer Science and Information Engineering, Graduate Institute of Biomedical Electronics and Bioinformatics, National Taiwan University, Taipei 10617, Taiwan

Kuang-Che Chang-Chien
Department of Computer Science and Information Engineering, National Chung Cheng University, Chiayi 621, Taiwan

Etsuo Takada
Division of Medical Ultrasonics, Center of Optical Medicine, Dokkyo Medical University School of Medicine, Mibu, Japan

Chiun-Sheng Huang
Department of Surgery, National Taiwan University Hospital and College of Medicine, National Taiwan University, Taipei, Taiwan

Yi-Hong Chou
Department of Radiology, Taipei Veterans General Hospital, National Yang Ming University School of Medicine, Taipei, Taiwan

Chen-Ming Kuo
Department of Computer Science and Information Engineering, National Chung Cheng University, Chiayi 621, Taiwan

Jeon-Hor Chen[a)]
Department of Radiology, China Medical University Hospital, Taichung, Taiwan

Purpose: Breast ultrasound (US) is recently becoming more and more popular for detecting breast lesions. However, screening results in hundreds of US images for each subject. This magnitude of images can lead to fatigue in radiologist, causing failure in the detection of lesions of a subtle nature. In this study, an image stitching technique is proposed for combining multipass images of the whole breast into a series of full-view images, and a fully automatic screening system that works off these images is also presented.
Methods: Using the registration technique based on the simple sum of absolute block-mean difference (SBMD) measure, three-pass images were merged into full-view US images. An automatic screening system was then developed for detecting tumors from these full-view images. The preprocessing step was used to reduce the tumor detection time of the system and to improve image quality. The gray-level slicing method was then used to divide images into numerous regions. Finally, seven computerized features—darkness, uniformity, width-height ratio, area size, nonpersistence, coronal area size, and region continuity—were defined and used to determine whether or not each region was a part of a tumor.
Results: In the experiment, there was a total of 25 experimental cases with 26 lesions, and each case was composed of 252 images (three passes, 84 images/pass). The processing time of the proposed stitching procedure for each case was within 30 s with a Pentium IV 2.0 processor, and the detection sensitivity of the proposed CAD system was 92.3% with 1.76 false positives per case.
Conclusions: The proposed automatic screening system can be applied to the whole breast images stitched together via SBMD-based registration in order to detect tumors. © *2010 American Association of Physicists in Medicine*. [DOI: 10.1118/1.3377775]

Key words: whole breast, ultrasound, computer-aided diagnosis (CAD) system, registration

I. INTRODUCTION

Breast cancer is globally one of the most common cancers among women. Early detection of breast cancer leads to a better chance of proper treatment.[1] Increased practice of mammographic screening has resulted in significant reduction in breast cancer mortality.[2,3] Mammography, however, is not sensitive for women with dense breast tissue, for whom ultrasound can really play a role in increasing the detection of occult cancers.[4–9] Sonography has recently been undergoing investigation as an alternative screening technique.[7–14] When combined with mammography, it has more sensitivity for screening women than using routine mammography alone.[9–11] Recently, a report[15] published by the American

College of Radiology Imaging Network (ACRIN) demonstrated the potential of ultrasound (US) in the screening of women at high risk of breast cancer. A multicenter trial was performed using a standardized technique and descriptive and interpretive criteria. The result of the trial provided guidance to participants and practitioners alike on the role of breast US.

Computer-aided diagnosis (CAD) offers a convenient and helpful reference opinion in the initial detection stage or a second reader once the physician has made an assessment.[16–18] With the CAD system, human oversights would be reduced, leading to more efficient and accurate diagnosis.[19] In previous studies,[20–23] several approaches with manual and automatic identification were proposed to efficiently detect breast lesions on US images. Madabhushi and Metaxas[20] proposed a method based on intensity and texture with empirical domain specific knowledge, along with directional gradient and a deformable shape-based model. Drukker and Giger[21] developed a computerized method based on the skewness of gray-level distribution to decrease limitation of posterior acoustic shadowing in tumor detection. Mogatadakala *et al.*[22] extracted order statistic features from multiresolution decompositions of energy-normalized subregions and thus automated detection and segmentation of suspicious regions in ultrasound B scans. Also, Chen *et al.*[23] exploited normalized cut and constrained grouping algorithms for breast tumor boundary detection in ultrasound images. However, these approaches were applied on two-dimensional (2D) US images with known tumor presence and therefore were not suitable for screening purpose. Recently, Ikedo *et al.*[24] proposed a CAD system to detect masses in the whole breast US images. The system employed two features including the edge direction and the density difference to detect masses in a US image. In this paper, we present a novel CAD system that automatically detects the suspicious slices from a series of 2D US images in a scan. Based on our preliminary result,[25] further comparison and analysis should be completed by additional experiments with tumor criteria. The aim of this study is to detect suspicious slices with tumors and further to locate the tumors.

Given the width of the standard US probe, several scanning passes are typically required to image an entire breast. Being able to convert adjacent passes into a single full-view breast image would be greatly beneficial for further US screening. There are a number of studies[26–29] that have examined image registration on US images, but the algorithms used in these studies have only focused on small three-dimensional (3D) volume images, not on full-view images, which would offer more information. Gee *et al.*[26] generated an alternative registration technique based on the sum of absolute difference (SAD) to integrate multiple freehand sweeps into larger images. In this paper, we present an image stitching technique based on the sum of absolute block-mean difference (SBMD) measure, which was modified from the SAD, to merge three-pass images into a full-view US image. The success of this technique enables the automatic detection of breast lesions based on a large set of imaging data.
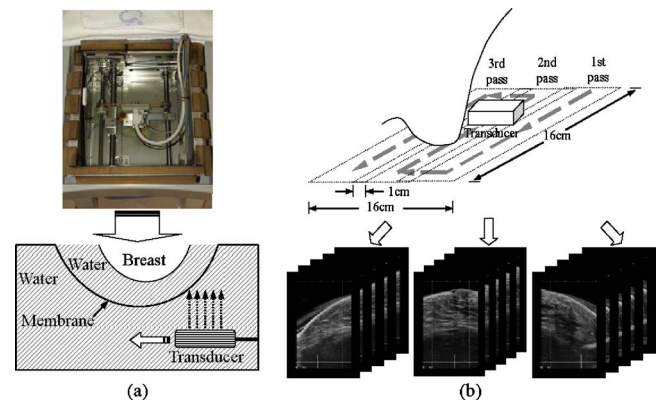
FIG. 1. The scanning procedure of the US machine. (a) An SSD-5500 US machine with a 6 cm linear transducer ASU-1004 (top). A US membrane separated water in a tank into the breast side (subtank) and the tank side (main tank). A breast was in the subtank, and a transducer immersed and moved mechanically in the main tank. (b) An entire breast was projected within an area of 16×16 cm^2, including three overlapping passes. Note that a subject bent down to position her breast in prone orientation (nipple down), but the images in Fig. 4 were presented in a supine orientation (nipple up).

II. MATERIALS AND METHODS

II.A. Data acquisition

In this paper, 25 female subjects with 26 breast lesions were studied. Of the 26 lesions, 9 were malignant in the biopsy result. The remaining 17 lesions were diagnosed as benign lesions through biopsy or with at least 2 yr of follow-up without evidence of change in echogenecity and lesion size. All the cases were acquired between May 2002 and April 2003 in the Center of Medical Ultrasonics, Dokkyo Medical University, Mibu, Japan. The recruited subjects were patients referred for breast sonography examination without special "selection criteria," with ages ranging from 25 to 73 yr old. The whole breast US images were scanned by using an SSD-5500 US machine with a 6 cm linear transducer ASU-1004 (Aloka, Japan). The frequency range was 5–10 MHz, and the center frequency was set at 7.5 MHz by the radiologist for all the cases. Also, the time gain compensation (TGC) settings and the dynamic range were set in advance and were fixed. Figure 1(a) shows a whole breast US scanning device. A transducer immersed into a water tank, and a special US membrane separated water into two parts, the breast side and the transducer side, for hygienic reasons. The material used for the 0.15 mm membrane is latex rubber, and the membrane does not cause echoes or artifacts. For scanning, a female subject had to bend down to position her breast in the subtank, and then the transducer would move and scan mechanically. Three passes were needed to project an entire breast within an area of 16×16 cm^2, where the overlap (O_{ML} and O_{MR}) between two passes was 1 cm, as shown in Fig. 1(b). Each pass included 84 images, and a total of 252 images was obtained with an interval of 2 mm between each image. Two focal zones were set at 1.5–2.5 and 4.5–5.5 cm, depending on the breast size, and the pixel resolution was 44 pixels/cm.
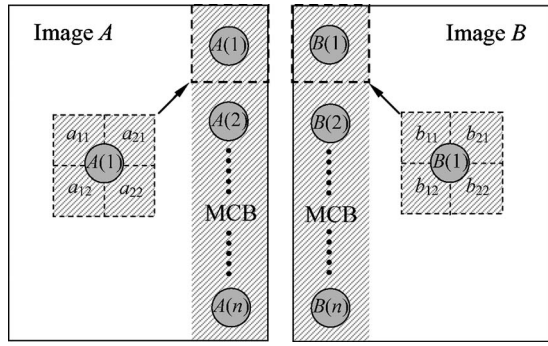
FIG. 2. The concept of sum of absolute block-mean difference (SBMD). $A(i)$ is the mean pixel of 2×2 block in image A and $B(i)$ is the mean pixel of 2×2 block in image B.
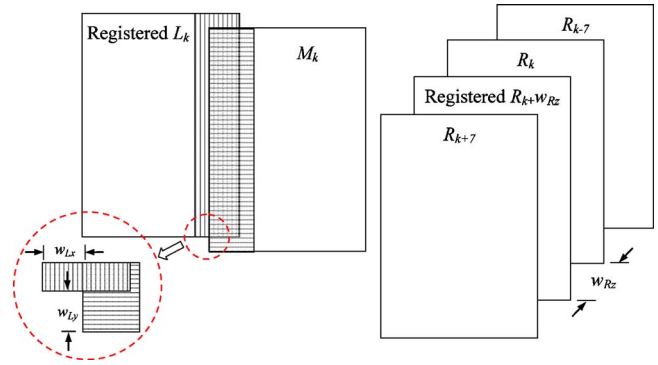

FIG. 3. The translation parameters in x (w_{Lx}), y (w_{Ly}), and z (w_{Rz}) coordinates on a stitching result of L_k, M_k, and R_k.

II.B. Image stitching procedure

These US image slices S_s, $1 \leq s \leq 252$, were separated into left frames L_k (pass 3), middle frames M_k (pass 2), and right frames R_k (pass 1), $1 \leq k \leq 84$. The scanning direction of pass 2 was different from other passes, as shown in Fig. 1(b). Therefore, the relation of L_k, M_k, and R_k to S_s is defined as

$$R_k = S_k, \quad M_k = S_{169-k}, \quad L_k = S_{k+168}, \quad 1 \leq k \leq 84. \quad (1)$$

When the patient movement was not considered, a significant issue during scanning, the ideal frame triplets, $\{L_k, M_k, R_k\}$, were easily obtained according to the relative position of each pass. The two overlapping regions (O_{ML} and O_{MR}) were then recorded by spatial registration and temporal alignment to obtain the final stitching result.

II.B.1. Spatial registration algorithm

In this step, the SBMD, a novel metric measure, was proposed to estimate the matching degree between two images. The main idea of SBMD is modified from the SAD,[26] which is calculated by

$$SAD = \sum_{i}^{N_p} |A_i - B_i|, \quad (2)$$

where N_p is number of pixels in the overlap region of images A and B, A_i is the ith pixel of image A, and B_i is the ith pixel of image B. In the SBMD measure, a mean calculated with pixels in a 2×2 block of the overlapping region is used instead of a single pixel value. The mean column block (MCB) is defined as a set of means, which are calculated with 2×2 blocks in the overlap region within the same image. Hence, the SBMD equation is defined as

$$SBMD = \sum_{i}^{N_b} |A(i) - B(i)|, \quad (3)$$

where N_b is the number of 2×2 blocks, $A(i)$ is defined as the mean of the ith 2×2 block in the overlapping region within image A, and $B(i)$ is defined the same as $A(i)$. The concept of the SBMD measure is illustrated in Fig. 2. In the SBMD measure, the matching degree of the estimation is similar to that of the SAD measure; that is, if the metric value is closer to zero, a superior registration result would be obtained. When the block means of two corresponding points in the overlap region are equal, the SBMD value is equal to 0.

Spatial registration was used to find the optimal match between the overlapping regions of two images that had the same frame number. If M_k was the fixed image and L_k was the moving image, then the SBMD measure is to evaluate the degree of matching between the overlap region of image M_k and image L_k. Let M_k^{ML} be the MCB in the middle-left overlap region O_{ML} of the fixed image M_k and L_{kj}^{ML} be one of the MCBs in the middle-left overlap region O_{ML} of the moving image L_k, $1 \leq j \leq N_{MCB}$, where N_{MCB} was the total number of the MCBs in the middle-left overlap region O_{ML} of the moving image L_k. According to Eq. (3), the SBMD stitching equation can be revised as

$$SBMD(M_k^{ML}, L_{kj}^{ML}) = \sum_{i}^{N_b} |M_k^{ML}(i) - L_{kj}^{ML}(i)| \quad \text{for } 1 \leq j$$

$$\leq N_{MCB}, \quad (4)$$

where $M_k^{ML}(i)$ is the ith block mean in M_k^{ML}, $L_{kj}^{ML}(i)$ is the ith block mean in L_{kj}^{ML}, and N_b is the number of the block means. Then, image stitching was needed to find the minimum metric criterion $SBMD(M_k^{ML}, L_{kj}^{ML})$ with respect to the various possible translation parameters. In this image stitching procedure, the possible parameters were translated by w_{Lx} pixels in the x coordinate and w_{Ly} pixels in the y coordinate. The translation parameters in the x and y coordinates for the $\{M_k, L_k\}$ pair were illustrated in Fig. 3. A similar definition was applied to the $\{M_k, R_k\}$ pair. So, the modified equation for the $\{M_k, R_k\}$ pair is

$$SBMD(M_k^{MR}, R_{kj}^{MR}) = \sum_{i}^{N_b} |M_{kr}^{MR}(i) - R_{kj}^{MR}(i)| \quad \text{for } 1 \leq j$$

$$\leq N_{MCB}, \quad (5)$$

where M_k^{MR} and R_{kj}^{MR} are similarly defined as Eq. (4) and are the middle-right overlap regions of image M_k and image R_k, respectively. The corresponding translation parameters $\{w_{Rx}, w_{Ry}\}$ are also obtained. Figure 4(a) shows a stitching result produced using the spatial registration algorithm.
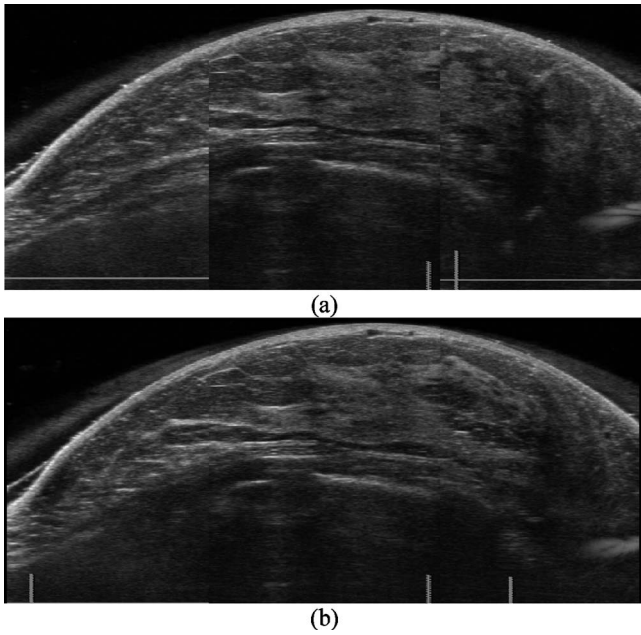
(a)

(b)

FIG. 4. (a) A stitching result after applying the spatial registration algorithm and (b) a stitching result after adding the temporal alignment step. Note that vertical line segments indicated the slice position in a pass.

II.B.2. Temporal alignment step

In actuality, there are many factors that may cause patient movement during scanning, such as heartbeat and respiration. In order to exclude such factors, the stitching procedure first undergoes temporal alignment before implementing the spatial registration procedure. In the temporal alignment step, the left ideal frame for the middle frame M_k would be selected from the frames $L_{k-7}, L_{k-6}, \ldots, L_k, \ldots, L_{k+6}, L_{k+7}$, and the right ideal frame would be selected from the frames $R_{k-7}, R_{k-6}, \ldots, R_k, \ldots, R_{k+6}, R_{k+7}$. For each frame pair $\{L_{k+m}, M_k, R_{k+n}\}$, $-7 \le m \le 7$ and $-7 \le n \le 7$, the minima of the metric $\mathrm{SBMD}(M_k^{\mathrm{ML}}, L_{(k+m)j}^{\mathrm{ML}})$ and $\mathrm{SBMD}(M_k^{\mathrm{MR}}, R_{(k+n)j}^{\mathrm{MR}})$ from Eqs. (4) and (5) are defined as

$$\mathrm{SBMD}(M_k^{\mathrm{ML}}, L_{mj}^{\mathrm{ML}}) = \min_{m=-7}^{7}\{\mathrm{SBMD}(M_k^{\mathrm{ML}}, L_{(k+m)j}^{\mathrm{ML}})\}$$

and

$$\mathrm{SBMD}(M_k^{\mathrm{MR}}, R_{nj}^{\mathrm{MR}}) = \min_{n=-7}^{7}\{\mathrm{SBMD}(M_k^{\mathrm{MR}}, R_{(k+n)j}^{\mathrm{MR}})\}. \quad (6)$$

After Eq. (6), the translation parameters in the z coordinate, w_{Lz} and w_{Rz}, were obtained, whose values are $m_k - k$ and $n_k - k$, respectively. The translation parameter w_{Rz} in the z coordinate for the $\{M_k, R_k\}$ pair was illustrated in Fig. 3. A stitching result produced using spatial and temporal alignment algorithms is shown in Fig. 4(b) and is more satisfactory for visual inspection than the result in Fig. 4(a).

II.C. Automatic screening system

After the image stitching procedure, 252 partial images of a case would be merged into 84 full-view US images. Then, a fully automatic screening system would attempt to detect
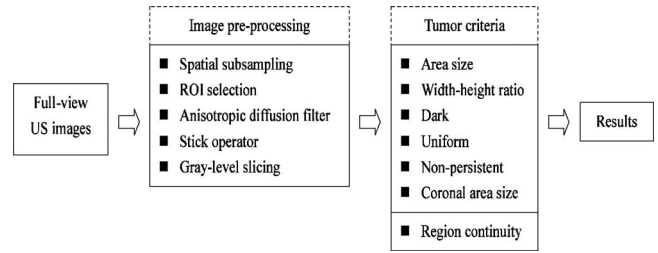
FIG. 5. The flowchart for the automatic screening system. The stitched US images were processed with preprocessing for quality enhancement and then were segmented by using gray-level slicing. Finally, seven criteria were used to detect tumorlike regions.

tumorlike regions in these images. The flowchart of the automatic screening procedure is shown in Fig. 5.

II.C.1. Image preprocessing step

In order to reduce processing time, in the spatial domain, a bilinear interpolation[30] was used to calculate a sampling value using the relationship of distance among the given pixel values. Then, some image preprocessing techniques, such as the anisotropic diffusion filter and the stick operator, were applied to reduce speckle noise and to enhance the contour of a lesion.

US images typically exhibit strong speckle noise because of the occurrence of wave interference that is inherent to any coherent imaging process.[31] The speckle noise degrades the image quality and makes it difficult to analyze image features. For this reason, we needed to perform relevant preprocessing steps in the automatic screening system. There are several low-pass filters, such as median filters[30] and averaging filters,[30] which are adopted for reducing US image noise. Although these methods may efficiently reduce noise, the boundary information and texture patterns, which are important to segmentation and feature extraction, are blurred in the process. Hence, in order to reduce noise while preserving object information, we used the anisotropic diffusion filter[32,33] to eliminate the speckle noise. The local image gradient was used to control anisotropic diffusion and to modify the classical isotropic diffusion equation into an anisotropic diffusion equation, represented by the formula

$$\frac{\partial I(x,y,t)}{\partial t} = \mathrm{div}[g(\|\nabla I\|) \cdot \nabla I], \quad (7)$$

where $\|\nabla I\|$ is the gradient magnitude, div is the divergence operator, $\| \|$ denotes the magnitude, and $g(\|\nabla I\|)$ is an edge-stopping function. This function is chosen to satisfy $g(x) \rightarrow 0$ when $x \rightarrow \infty$ and should be monotonically decreasing so that the diffusion decreases as the gradient strength increases and stops across the edges.

After the anisotropic diffusion filtering step, the stick, a line segment of variable orientation, was used to reduce speckle and to enhance edge information.[34,35] In the conception of the stick method, let a given square area of size be $N_S \times N_S$ in an image, then $2N_S - 2$ lines of length N_S pixels can be drawn through the center of square area. The sum of
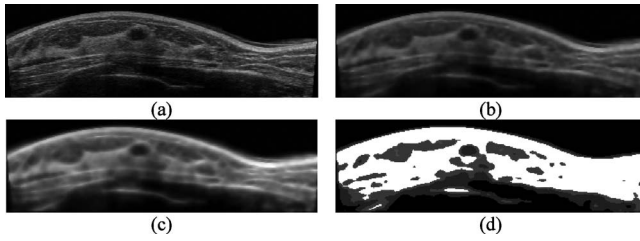
FIG. 6. The results of three preprocessing. (a) An original US image. (b) The result after applying the anisotropic diffusion filter to (a). (c) The result after applying the stick operator (5×5 mask) to (b), and (d) the result after applying gray-level slicing to (c).

288 the pixel values on the same line is calculated for each line.
289 Then the maximum of these sums is selected. After each
290 pixel in an image is replaced by the maximum sum of the
291 lines passing through that pixel, edge contrast is enhanced
292 and speckle is reduced. In this paper, we set $N_S = 5$.

293 II.C.2. Image segmentation

294   In US images, the distribution of gray levels over differ-
295 ent breast tissues is inconsistent. Generally, regions of cyst
296 and tumor, desirable areas of detection in this study, were
297 darker than the fat tissue.[36] Therefore, we used a simple
298 thresholding method, gray-level slicing,[30] to divide gray lev-
299 els into four ranges. The gray-level ranges were selected us-
300 ing five cases in advance, and better results were obtained
301 when four ranges were set to 0–26, 27–42, 43–71, and 72–
302 255, respectively. The first range includes cysts; the second
303 and third ranges represent the suspicious tissues; and the last
304 range includes all the other tissues, i.e., fibrous tissues, glan-
305 dular tissues, and calcifications. The selected ranges were
306 used only for cases scanned based on the fixed TGC settings
307 and the dynamic range. In the current method, the cysts and
308 mass regions would be detected at the same time because
309 they are darker than fat. This paper is focused on the detec-
310 tion, and the further differentiation of cysts and mass regions
311 could be conducted by the other methods.
312   Finally, pixels associated with gray levels in the same
313 range were replaced by the average of the pixels. The re-
314 sulted image from the application of all preprocessing algo-
315 rithms is shown in Fig. 6.

316 II.C.3. Definition of tumor criteria

317   After image preprocessing, an image was divided into
318 several regions. A region would be determined as a tumorlike
319 region if it satisfied the predefined criteria of area size,
320 width-height ratio, darkness, uniformity, nonpersistence,
321 coronal area size, and region continuity.
322   *II.C.3.a. Area size.* Because of the influence of noise on
323 US, lots of regions with a very small area would be produced
324 after applying the segmentation method. Hence, the area size
325 criterion was defined for excluding useless regions such as
326 those due to noise. The area of each region must satisfy

$$\text{area}_R > \text{TH}_{\text{area}}, \tag{8}$$

where area_R is the total pixel number in the region and TH_{area}
is a predetermined area threshold.

   II.C.3.b. Width-height ratio. The shape of a tumor is
rarely flat and elongated.[14] Therefore, the width-height ratio
criterion was used to eliminate the regions with a flat and
elongated shape. Each region was first enclosed by a closest
bounding rectangle, and then the width-height ratio R_{WH} of
the rectangle was calculated by

$$\begin{cases} R_{WH} = \dfrac{W_R}{H_R} & \text{if } H_R > W_R \\[2mm] R_{WH} = \dfrac{H_R}{W_R} & \text{otherwise}, \end{cases} \tag{9}$$

where W_R and H_R are the width and height of the suspicious
region. The width-height ratio must satisfy

$$R_{WH} > \text{TH}_{WH}, \tag{10}$$

where TH_{WH} is a predetermined width-height threshold. If
R_{WH} is equal or smaller than TH_{WH}, this region would be
excluded.

   II.C.3.c. Darkness. Tumors are usually darker than normal
tissue in US images. In addition, cysts are darker than
tumors.[36] According to this property, nontumor regions can
then be excluded if their gray levels are not dark enough.
Hence, the average gray level GL_{avg} of each suspicious re-
gion can be calculated by the following equation:

$$\text{GL}_{\text{avg}} = \frac{\sum \text{GL}_R(x,y)}{N_{\text{pixel}}}, \tag{11}$$

where $\text{GL}_R(x,y)$ is the gray level of pixel (x,y) and N_{pixel} is
the number of pixels in the suspicious region. Then, the dark-
ness criterion is defined as

$$\text{GL}_R < \text{TH}_{\text{GL}}, \tag{12}$$

where TH_{GL} is the predetermined darkness threshold value.

   II.C.3.d. Uniformity. In general, a part within a tumor is
often uniform in its gray level; therefore, gray levels of pix-
els in the suspicious region are similar.[36] The variance Var_R
of a region can be calculated by the intensity difference be-
tween each pixel and the regional mean value in the follow-
ing equation:

$$\text{Var}_R = \frac{\sum (\text{GL}_R(x,y) - \text{GL}_{\text{avg}})^2}{N_{\text{pixel}} - 1}, \tag{13}$$

where GL_{avg} is defined in Eq. (11) and N_{pixel} is the number of
pixels in the suspicious region. A uniform region must satisfy

$$\text{Var}_R < \text{TH}_{\text{uniform}}, \tag{14}$$

where $\text{TH}_{\text{uniform}}$ is the predetermined uniform threshold.

   II.C.3.e. Nonpersistence. The nonpersistence criterion was
defined by removing nontumor tissue with a background im-
age constructed from several consecutive images. The back-
ground image was produced based on the image averaging
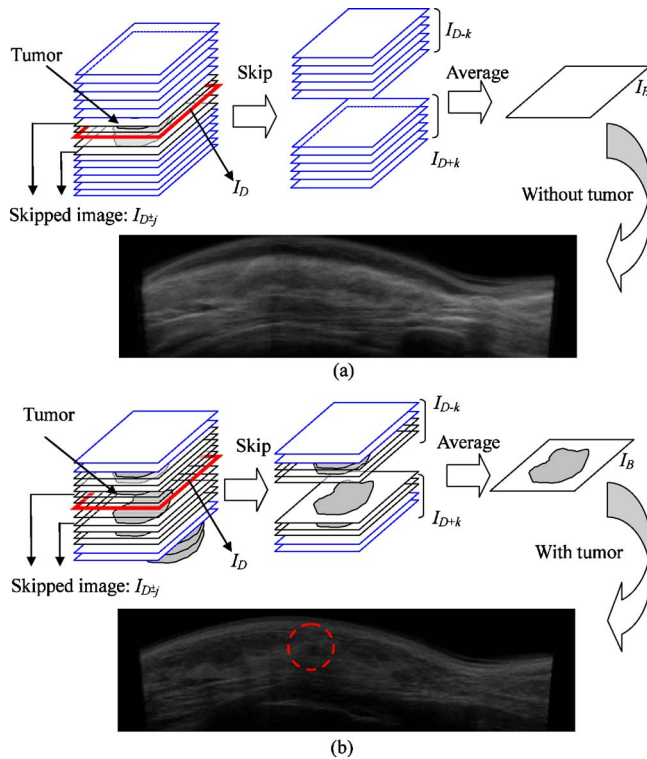technique[30] and was used for comparing with the detected

(a)

(b)

FIG. 7. (a) If the number of skipped images is large enough to include all the tumor frames, the background image I_B would be without tumor. (b) If the number of skipped images is less, the background image I_B would include tumor indicated by a circle.

image.

Let I_D be a current detected image. First, the previous (and following) m images nearby I_D, which might contain tumor regions, were denoted as $I_{D\pm p}$, for $1 \le p \le a$. Totally, $2a+1$ images were skipped. Then, the background image I_B was obtained from the average of images which included the $(b-a)$ previous and $(b-a)$ following images nearby $I_{D\pm p}$, and were denoted as $I_{D\pm q}$, for $a+1 \le q \le b$. The gray level of each pixel on I_B can be calculated as

$$I_B(x,y) = \frac{\sum I_{D\pm q}(x,y)}{2(b-a)}. \tag{15}$$

The number of skipped images must be large enough to exclude the whole tumor. Figure 7(a) shows that the background image was constructed with the sufficient number of skipped images $I_{D\pm p}$; therefore, there is no tumorlike tissue in the background I_B. Figure 7(b) shows the number of skipped images was insufficient so that there were several images with tumor among I_{D-q} and I_{D+q}. The background image, which is produced by averaging images, I_{D-q} and I_{D+q}, would be with a tumor region, indicated by an ellipse, making it difficult to notice the difference between the current detected images and the background image. In this paper, the parameters were selected as $a=5$ and $b=10$ by discussing with the radiologist. After the background image I_B is produced, for a coordinate (x,y) within the detecting region on I_D, the gray-level contrast between two corresponding pixels on I_D and I_B can be calculated by
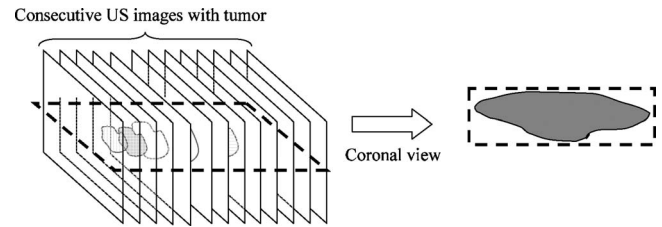

FIG. 8. An overview of coronal view. A coronal-view image was produced from a cross section of consecutive US images.

$$C_{x,y} = \frac{I_D(x,y) - I_B(x,y)}{\sqrt{\dfrac{1}{2(b-a)} \displaystyle\sum^{q} (I_{D\pm q}(x,y) - I_B(x,y))}}. \tag{16}$$

By this formula, the influence of the noise is reduced. Hence, the difference between I_D and I_B can be calculated by

$$\overline{C_R} = \frac{1}{N_{\text{pixel}}} \sum C_{x,y}, \tag{17}$$

where N_{pixel} is the total pixel number of the region. Hence, the region is excluded if

$$\overline{C_R} < \text{TH}_C, \tag{18}$$

where TH_C is a predetermined nonpersistent threshold.

II.C.3.f. Coronal area size. In general, the coronal shape of a tumor is approximate to a dark ellipse, and the area of the coronal region is usually larger than other nontumor tissues. This property can be used to exclude nontumor tissues with small coronal area. Hence, a coronal-view image was produced from a cross section of consecutive US images at a designated depth. Figure 8 shows an example for construction of a coronal-view image produced form consecutive US images with tumor. Let area_T be the tumor region size in the coronal view image and area_{Cr} is the coronal view image size. The ratio R_{CA} between the area of the tumor region and the area of the coronal image is calculated by

$$R_{CA} = \frac{\text{area}_T}{\text{area}_{Cr}}. \tag{19}$$

The area ratio R_{CA} is then compared to a predetermined threshold. If it is smaller than the threshold TH_{CA}, this corresponding region is excluded.

II.C.3.g. Region continuity. In Figs. 9(b)–9(g), we show the individual results after applying each of the six tumor criteria. Note the regions that did not satisfy the criteria were displayed in white pixels. As shown, almost all normal regions could be excluded by using the first six criteria. The final region satisfying all six tumor criteria is shown in Fig. 9(g) and was labeled as a suspicious region with possible tumor.

In general, a tumor is an irregular solid mass within the breast that is typically shown across serial images. Therefore, the possibility that the region in the current image contains a tumor increases significantly if its corresponding region in the succeeding image also satisfies the six tumor criteria. This procedure is called the region continuity criterion. In
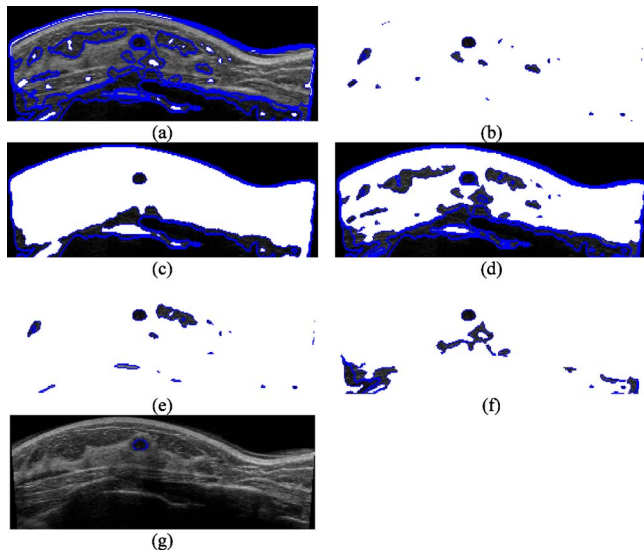
FIG. 9. The results respectively show regions satisfied (a) the area size criterion, (b) the width-height ratio criterion, (c) the gray-level criterion, (d) the uniform criterion, (e) the irregular region criterion, and (f) the coronal area size criterion. Finally, a region satisfied six tumor criteria is shown in (g).
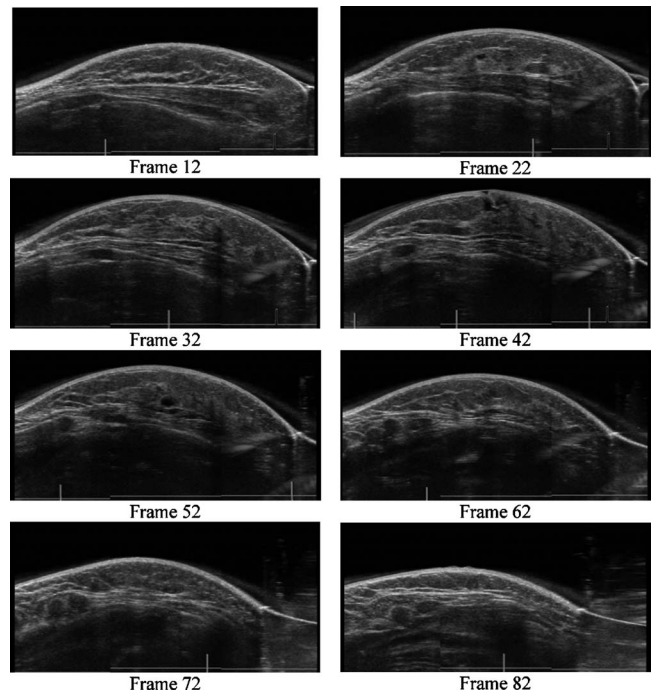

FIG. 11. Eight stitched results of all stitched results (84 frames) in case 1.

435 Fig. 10, there are three possible suspicious regions, *b*, *c*, and
436 *d* in the current image, but only region *c* satisfies the region
437 continuity criterion because its corresponding region *e* in the
438 succeeding image is also labeled as a possible suspicious
439 region. This is to say that only region *c* satisfies all pre-
440 defined criteria, so it would be labeled as a truly suspicious
441 region.

III. RESULT
442

443   Most of the 25 cases in our experiments, the exception
444 being the ninth case with two lesions, had one lesion. Each
445 case was scanned and the images were stored as DICOM
446 files by the aforementioned US machine. After decoding the
447 DICOM files, cases consisting of 252 images (three passes,
448 84 images/pass) were processed with the proposed stitching
449 procedure and screening system. In this study, all the thresh-

olds for tumor criteria, after discussion with a radiologist, **450**
were selected as follows: $TH_{area}=60$, $TH_{WH}=0.5$, $TH_{GL}=55$, **451**
$TH_{uniform}=5$, $TH_C=14.7$, and $TH_{CA}=0.6$. **452**

III.A. Experimental protocol and results **453**

    The image stitching procedure was used to combine the **454**
three-pass US images into full-view images. In Fig. 11, 8 out **455**
of the 84 stitched results from case 1 are shown. The pro- **456**
cessing time of the stitching procedure by a Pentium IV 2.0 **457**
processor for each case (252 images) was within 30 s. With a **458**
focus on accuracy of tumor detection, a simple evaluation **459**
protocol, namely, mean square error (MSE), was used to **460**
evaluate the performance of the proposed stitching method. **461**
The MSE of the overlapping region is calculated by **462**

$$MSE = \frac{1}{N_O}\sum_{r=1}^{N_O} (A_r - B_r)^2, \qquad (20)$$
463

where A and B are the overlapping regions, N is the total **464**
pixel number of the overlapping region, A_r is one of pixels in **465**
the overlapping region A, and B_r is the similar definition of **466**
B. In Fig. 12, four enlarged images obtained from four **467**
frames in case 1 were used to show the stitching parts with **468**
different MSE values; that is, in Figs. 12(a), 12(b), and **469**
12(d), the MSE values of the left stitching result of frames **470**
22, 32, and 82 were 104, 234, and 1520, respectively, and the **471**
MSE value of the right stitching result of frame 52 was 893. **472**
Figure 13 shows all MSE values of the left and right stitch- **473**
ing results in case 1 using two statistical curves. Note that **474**
the red curve is for MSE values of the left stitching results **475**
and the blue line is for the right stitching results. **476** AQ: #2

    With stitched full-view images, each experimental case **477**
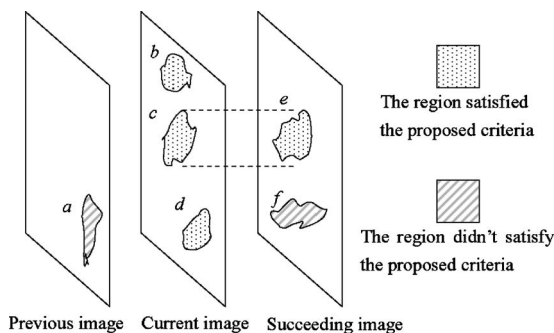was diagnosed by the proposed CAD system. Diagnoses **478**

FIG. 10. The illustration of the region continuity criterion. In the current image, region *b*, *c*, and *d* satisfy the first six criteria, but only region *c* satisfies the region continuity criterion because its corresponding region *e* in the succeeding image is also labeled as a possible suspicious region.
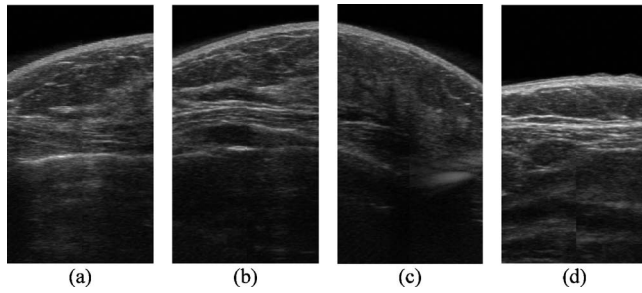
FIG. 12. Four enlarged images for the stitching parts of four frames in case 1. (a) In frame 22, the MSE value of the left stitching result was 104, (b) in frame 32, the MSE value of the left stitching result was 234, (c) in frame 52, the MSE value of the right stitching result was 893, and (d) in frame 82, the MSE value of the left stitching result was 1520.
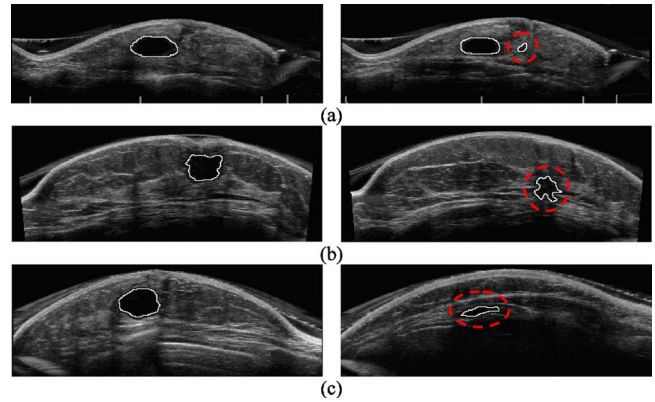

FIG. 14. (a) case 2, (b) case 5, and (c) case 11 show three examples of the true positive frames (the left side images) and three examples of the false positive frames (the right side images).

made by a physician with 10 yr of experience in breast imaging were compared with experimentally derived conclusions. Figure 14(a) shows two diagnosed results of case 2: The left image is a true positive frame and the right image is a false positive (FP) frame (the false positive region is indicated by an ellipse). The true and false positive frames of cases 5 and 11 are also shown in Figs. 14(b) and 14(c), respectively. Out of the 25 cases with 26 lesions, our CAD system missed 2 lesions, one each from cases 15 and 23. Figure 15 shows two false negative frames in cases 15 and 23. In Fig. 16, the free-response operating characteristic (FROC) (Ref. 37) curve shows the performance of the proposed screening system. In order to generate the FROC curve, the threshold value TH_{WH} was changed in the width-height ratio criterion. The CAD scheme yielded a detection sensitivity of 92.3% (24/26 lesions) with 1.76 FPs/case.

III.B. Discussion

Breast cancer is the second leading cause of carcinogenic death in women behind lung cancer.[1] In America, one in eight women will be diagnosed with this deadly disease, and an estimated 192 370 new cases of invasive breast cancer will be diagnosed among women this year.[1] In an attempt to reduce mortality rates, breast US has recently become more and more popular for detecting breast lesion in early stages.[4–9]

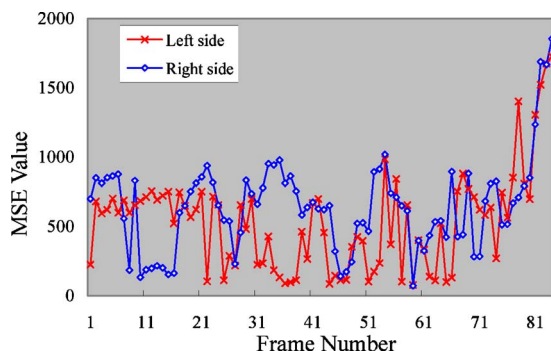The CAD system's use as a reference opinion for improving accuracy and reliability of diagnosis has attracted much interest among researchers over the past decade. Previous studies focused on two key areas: The detection of the tumor region[22,38–41] and the classification of breast masses.[42–46] For boundary extraction of breast masses, Cary *et al.*[38] used leak properties to grow a manually drawn seed region close to the tumor boundary. Yap *et al.*[39] exploited hybrid filtering, multifractal processing, and thresholding segmentation to initially detect the tumor region. In classification, Sahiner *et al.*[42] extracted two morphological and six texture features from a given segmentation on US for evaluation of tumors. Huang *et al.*[43] quantified tumor vascularity on 3D power Doppler. In these studies, although various degrees of success have been achieved, all the approaches were applied on a breast US image associated with known tumor presence.

Ikedo *et al.*[24] proposed a CAD system to automatically detect masses using the whole breast US images. The detection sensitivity of the CAD system was 80.6% (29/36 lesions). However, at the edge detection step, several FPs were generated due to breast anatomy Vertical edges would also be detected near areas of Cooper's ligaments and ribs. Their method also had difficulty detecting flat-shaped masses because poor near-vertical edges were difficult to determine using edge detection. In our study, seven criteria were used to distinguish images with suspicious tumors from US images without tumors. The detection sensitivity of our system was improved by basing our determination on evaluation of the region not affected by Cooper's ligaments and ribs. The extracted features included 3D information, such as coronal-view criterion, which could increase detection sensitivity.

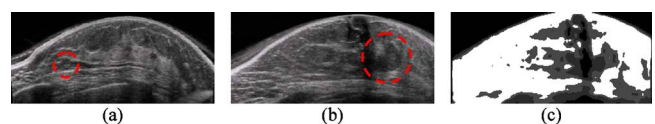FIG. 13. Two MSE statistical curves for the left and right stitching results in case 1.

FIG. 15. (a) A false negative frame in case 15, (b) a false negative frame in case 23, and (c) the poor segmentation result of (b). Two tumors were indicated by circles.
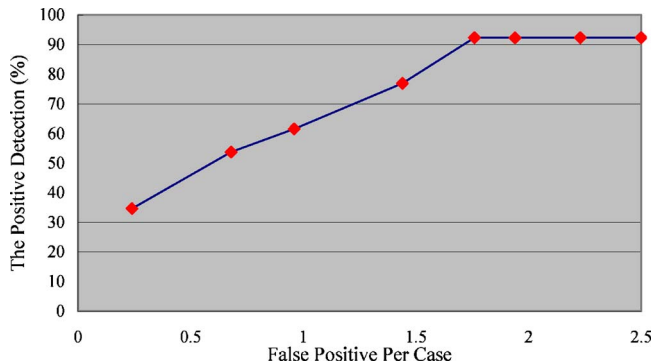
FIG. 16. FROC curves of the CAD scheme based on 25 cases.

according to the size of the tumor. Hence, all thresholds were [578] selected after discussion with the radiologist. With a focus on [579] differentiation between US images with and without tumors, [580] thresholds were used to exclude normal regions for finding [581] parts of tumor. [582]

From our results, we have found that the MSE values [583] estimated from the right sides of the last stitched frames were [584] larger than those estimated from the middle stitched frames, [585] as shown in Fig. 13; the MSE values for frames 81, 82, 83, [586] and 84, were 1234, 1687, 1667, and 1853 for the $\{M_k, R_k\}$ [587] pairs and 1304, 1520, 1675, and 1725 for the $\{M_k, L_k\}$ pairs. [588] This might be due to undesirable results from the temporal [589] alignment step; perhaps there may have been alternate left/ [590] right frame pairs $\{L_m, R_n\}$ with higher matching degrees with [591] the middle frame M_k. Fortunately, this problem did not [592] deeply affect the performance of the proposed system, as [593] image information in the first or the last frames is usually not [594] necessary nor important. Almost all important information is [595] usually contained within the middle stitched frames and thus, [596] we were able to ignore these estimative errors. [597]

Our results also showed that almost all the tumors or cysts [598] identified by the physician could also be detected through the [599] proposed screening system. In Fig. 14, three examples of the [600] true positive frames of cases 2, 5, and 11 are shown on the [601] left side; on the right side, three examples of the false posi- [602] tive frames of the same cases are shown. The determination [603] errors that we noticed were due to texture of the regions [604] represented like tumor tissue. This might be caused espe- [605] cially when an inappropriate operation was made in the scan- [606] ning procedure such as patient posture. In our study, only [607] two false negative diagnoses were noted. Infrequency of [608] false negativity, and thus accuracy, is very important for any [609] imaging system designed for automatic detection of lesions. [610] In Fig. 15, the false negative frames of cases 15 and 23 are [611] shown, and ellipses are used to indicate true locations of the [612] tumors. The tumor size in case 15 is so small (only 2.5 mm) [613] that it would not satisfy the area size criterion. In case 23, the [614] false negative region did not satisfy the width-height ratio [615] criterion because the pattern joined to the nipple shadow so [616] that the segmentation result was poor, as shown in Fig. 15(c). [617] There were also 44 detected false positives. Upon closer ob- [618] servation, it was discovered that all the false positive regions [619] were dark and uniform like the appearance of tumor regions, [620] as shown in the right side of Fig. 14. All of the suspicious [621] regions detected by the proposed CAD system were indeed [622] tumorlike regions. Therefore, the proposed system can in- [623] deed be used to find the suspicious frames from a series of [624] 2D US images that may or may not contain tumors. Since the [625] major role of the CAD system is to provide a reference opin- [626] ion in the initial diagnosis stage, the average 1.76 false posi- [627] tive marks per case in this study can further be checked and [628] easily verified for their nature of being malignant, benign, or [629] normal by the breast radiologist. [630]

[535] Generally, a breast screening scan of a patient includes [536] hundreds of US images. It is inefficient for the radiologist to [537] interpret this many scans. Fatigue and a subtle nature can [538] lead to a radiologist's failure in the detection of a lesion. [539] After obtaining full-view US images, an automatic screening [540] system was used to detect the presence of tumors. In order to [541] reduce processing time, the degree of image resolution was [542] first reduced by subsampling. Several preprocessing tech- [543] niques including the anisotropic diffusion filter[32,33] and the [544] stick operator[34,35] were applied to reduce speckle noise and [545] to enhance the edges in each US image. A thresholding al- [546] gorithm based on gray-level slicing[30] was then used to divide [547] the US image into numerous regions. Each region was de- [548] fined by the seven predefined criteria of darkness, uniformity, [549] width-height ratio, area size, nonpersistence, coronal area [550] size, and region continuity. Each region that satisfied these [551] criteria was labeled as a suspicious frame with possible tu- [552] mor presence. In order to increase efficiency and [553] effectiveness,[47] we propose a novel CAD system for sifting [554] suspicious slices from a series of 2D US images of a breast. [555] The CAD system would offer a convenient and helpful ref- [556] erence opinion in the initial detection stage or a second [557] reader once the physician has made assessment. The focus of [558] the system is to differentiate suspicious slices from other US [559] images in a scan.

[560] To have automatic tumor detection, US images in three [561] passes needed to be merged into a series of full-view images. [562] In our previous work,[25] we utilized an image stitching algo- [563] rithm to stitch multipass images into a full-view image. This [564] previous method was based on mutual information[48] regis- [565] tration and the results were evaluated by two metrics for [566] optimization—the sum of squared differences[49] and normal- [567] ized correlation. In the present paper, we focused on tumor [568] detection so that we employed a simpler algorithm (SBMD), [569] which was modified from a SAD algorithm, for image stitch- [570] ing. In the SBMD method, we calculated difference between [571] two 2×2 blocks in two images instead of the difference [572] between two pixels.

[573] In our study, each criterion used had an individual thresh- [574] old. There were no prior standards for determining the pre- [575] determined threshold, and it was difficult to train the pro- [576] posed criteria with US images. Several thresholds are related [577] to the tumor size and the users could change the thresholds

AQ: **#3**

IV. CONCLUSION [631]

In this study, we proposed a CAD system to automatically [632] detect tumors from a serial of 2D US images. By using im- [633]

age stitching based on the proposed SBMD measure, 252 US images of three passes were merged into 84 full-view images which offer more information than a stack of 2D US scans for beast diagnosis. The CAD scheme yielded a detection sensitivity of 92.3% (24 out of 26 lesions) with a total 44 false positives (1.76/case). Our study shows that the proposed system could automatically detect suspicious frames with tumorlike regions and it would be useful in diagnosis and efficiency improvement.

Although the developed system offered high detection sensitivity (92.3%), there were limitations in our study. For the adopted automated ultrasound system, the limited depth of penetration (deep lesions might be missed), shadowing by Cooper's ligaments, shadowing distal to lesions, and limited scan range (large breasts would be out of the scan range) would cause some breast tissue and potential lesions to be missed. A better method for standardization of system sensitivity settings would be needed in future studies. Using the current technique, the processing time for each case is still too long. In the future work, for time efficiency, processing times falling within 2 min/case should be decreased. Also, in this study, the high sensitivity was associated with 1.76 false positive marks per case due to segmentation results. An inaccurate segmentation result produced by a simple algorithm, such as gray-level slicing might adversely affect our conditional analysis. A superior algorithm should be exploited to precisely detect the contour of a pattern so that the number of false positive and false negative regions can be reduced. Moreover, more cases are acquired to find more reliable threshold values for adapting images with different settings. If the system can offer a more accurate and reliable diagnosis, its clinical practicality will be increased.

ACKNOWLEDGMENT

a)Author to whom correspondence should be addressed. Electronic mail: jeonhc@uci.edu

[1]*Breast Cancer Facts and Figures 2009* (American Cancer Society, Atlanta, GA, 2009).

[2]S. Buseman, J. Mouchawar, N. Calonge, and T. Byers, "Mammography screening matters for young women with breast carcinoma," Cancer **97**, 352–358 (2003).

[3]M. Funke and C. Villena, "Breast cancer imaging," Radiology **48**, 601–614 (2008).

[4]S. W. Chan, P. S. Cheung, S. Chan, S. S. Lau, T. T. Wong, M. Ma, A. Wong, and Y. C. Law, "Benefit of ultrasonography in the detection of clinically and mammographically occult breast cancer," World J. Surg. **32**, 2593–2598 (2008).

[5]V. Corsetti, A. Ferrari, M. Ghirardi, R. Bergonzini, S. Bellarosa, O. Angelini, C. Bani, and S. Ciatto, "Role of ultrasonography in detecting mammographically occult breast carcinoma in women with dense breasts," Radiol. Med. (Torino) **111**, 440–448 (2006).

[6]S. S. Kaplan, "Clinical utility of bilateral whole-breast US in the evaluation of women with dense breast tissue," Radiology **221**, 641–649 (2001).

[7]V. Corsetti, N. Houssami, A. Ferrari, M. Ghirardi, S. Bellarosa, O. Angelini, C. Bani, P. Sardo, G. Remida, E. Galligioni, and S. Ciatto, "Breast screening with ultrasound in women with mammography-negative dense breasts: Evidence on incremental cancer detection and false positives, and associated cost," Eur. J. Cancer **44**, 539–544 (2008).

[8]M. H. Dilhudy, "Assessment of the dense breast within the French screen-

ing program: The role of ultrasonography," J. Radiol. **89**, 1180–1186 (2008).

[9]K. Uchida, A. Yamashita, K. Kawase, and K. Kamiya, "Screening ultrasonography revealed 15% of mammographically occult breast cancers," Breast Cancer **15**, 165–168 (2008).

[10]W. A. Berg, J. D. Blume, J. B. Cormack, E. B. Mendelson, D. Lehrer, M. Böhm-Vélez, E. D. Pisano, R. A. Jong, W. P. Evans, M. J. Morton, M. C. Mahoney, L. H. Larsen, R. G. Barr, D. M. Farria, H. S. Marques, and K. Boparai, "Combined screening with ultrasound and mammography vs mammography alone in women at elevated risk of breast cancer," JAMA, J. Am. Med. Assoc. **299**, 2151–2163 (2008).

[11]E. Tohno, E. Ueno, and H. Watanabe, "Ultrasound screening of breast cancer," Breast Cancer **16**, 18–22 (2009).

[12]A. Tardivon, "Screening ultrasound of breast cancer in a high-risk population," J. Radiol. **89**, 748–■ (2008).

[13]H. J. Shin, H. H. Kim, S. M. Kim, G. Y. Kwon, G. Gong, and O. K. Cho, "Screening-detected and symptomatic ductal carcinoma in situ: Differences in the sonographic and pathologic features," AJR, Am. J. Roentgenol. **190**, 516–525 (2008).

[14]A. T. Stavros, D. Thickman, C. L. Rapp, M. A. Dennis, S. H. Parker, and G. A. Sisney, "Solid breast nodules: Use of sonography to distinguish between benign and malignant lesions," Radiology **196**, 123–134 (1995).

[15]W. A. Berg, E. B. Mendelson, C. R. B. Merritt, J. Blume, and M. Schleinitz, ACRIN 6666: Screening Breast Ultrasound in High-Risk Women, American College of Radiology Imaging Network, 2007.

[16]A. N. Karahaliou, I. S. Boniatis, S. G. Skiadopoulos, F. N. Sakellaropoulos, N. S. Arikidis, E. A. Likaki, G. S. Panayiotakis, and L. I. Costaridou, "Breast cancer diagnosis: Analyzing texture of tissue surrounding microcalcifications," IEEE Trans. Inf. Technol. Biomed. **12**, 731–738 (2008).

[17]S. M. Astley, "Computer-based detection and prompting of mammographic abnormalities," Br. J. Radiol. **77**, S194–S200 (2004).

[18]K. Horsch, M. L. Giger, C. J. Vyborny, and L. A. Venta, "Performance of computer-aided diagnosis in the interpretation of lesions on breast sonography," Acad. Radiol. **11**, 272–280 (2004).

[19]K. Drukker, C. A. Sennett, and M. L. Giger, "Automated method for improving system performance of computer-aided diagnosis in breast ultrasound," IEEE Trans. Med. Imaging **28**, 122–128 (2009).

[20]A. Madabhushi and D. N. Metaxas, "Combining low-, high-level and empirical domain knowledge for automated segmentation of ultrasonic breast lesions," IEEE Trans. Med. Imaging **22**, 155–169 (2003).

[21]K. Drukker and M. L. Giger, "Computerized analysis of shadowing on breast ultrasound for improved lesion detection," Med. Phys. **30**, 1833–1842 (2003).

[22]K. V. Mogatadakala, K. D. Donohue, C. W. Piccoli, and F. Forsberg, "Detection of breast lesion regions in ultrasound images using wavelets and order statistics," Med. Phys. **33**, 840–849 (2006).

[23]S. Y. Chen, H. H. Chang, S. H. Hung, and W. C. Chu, "Breast tumor identification in ultrasound images using the normalized cuts with partial grouping constraints," International Conference on Biomedical Engineering and Informatics, 2008, Vol. 2, pp. 28–32 (unpublished).

[24]Y. Ikedo, D. Fukuoka, T. Hara, H. Fujita, E. Takada, T. Endo, and T. Morita, "Development of a fully automatic scheme for detection of masses in whole breast ultrasound images," Med. Phys. **34**, 4378–4388 (2007).

[25]R. F. Chang, C. J. Chen, E. Takada, C. M. Kuo, and D. R. Chen, "Image stitching and computer-aided diagnosis for whole breast ultrasound image," in CARS 2006: Computer Assisted Radiology and Surgery, Osaka, Japan, 2006, Vol. 1, pp. 330–343 (unpublished).

[26]A. H. Gee, G. M. Treece, R. W. Prager, C. J. Cash, and L. Berman, "Rapid registration for wide field of view freehand three-dimensional ultrasound," IEEE Trans. Med. Imaging **22**, 1344–1357 (2003).

[27]R. Shekhar, V. Zagrodsky, M. J. Garcia, and J. D. Thomas, "Registration of real-time 3-D ultrasound images of the heart for novel 3-D stress echocardiography," IEEE Trans. Med. Imaging **23**, 1141–1149 (2004).

[28]G. P. Penney, J. M. Blackall, M. S. Hamady, T. Sabharwal, A. Adam, and D. J. Hawkes, "Registration of freehand 3D ultrasound and magnetic resonance liver images," Med. Image Anal. **8**, 81–91 (2004).

[29]C. J. Chen, R. F. Chang, W. K. Moon, D. R. Chen, and H. K. Wu, "2-D ultrasound strain images for breast cancer diagnosis using nonrigid subregion registration," Ultrasound Med. Biol. **32**, 837–846 (2006).

[30]R. C. Gonzalez and R. E. Woods, *Digital Image Processing*, 3rd ed. (Prentice-Hall, Englewood Cliffs, NJ, 2007).

[31]O. V. Michailovich and A. Tannenbaum, "Despeckling of medical ultra-

sound images," IEEE Trans. Ultrason. Ferroelectr. Freq. Control **53**, 64–78 (2006).

[32]P. Perona and J. Malik, "Scale-space and edge detection using anisotropic diffusion," IEEE Trans. Pattern Anal. Mach. Intell. **12**, 629–639 (1990).

[33]S. Aja-Fernández and C. Alberola-López, "On the estimation of the coefficient of variation for anisotropic diffusion speckle filtering," IEEE Trans. Image Process. **15**, 2694–2701 (2006).

[34]R. N. Czerwinski, D. L. Jones, and W. D. O'Brien, "Line and boundary detection in speckle images," IEEE Trans. Image Process. **7**, 1700–1714 (1998).

[35]R. Munbodh, Z. Chen, D. A. Jaffray, D. J. Moseley, J. P. Knisely, and J. S. Duncan, "Automated 2D–3D registration of portal images and CT data using line-segment enhancement," Med. Phys. **35**, 4352–4361 (2008).

[36]L. Liberman and J. H. Menell, "Breast imaging reporting and data system (BI-RADS)," Radiol. Clin. North Am. **40**, 409–430 (2002).

[37]D. Chakraborty, "Statistical power in observer-performance studies: Comparison of the receiver operating characteristic and free-response methods in tasks involving localization," Acad. Radiol. **9**, 147–156 (2002).

[38]T. W. Cary, E. F. Conant, P. H. Arger, and C. M. Sehgal, "Diffuse boundary extraction of breast masses on ultrasound by leak plugging," Med. Phys. **32**, 3318–3328 (2005).

[39]M. H. Yap, E. A. Edirisinghe, and H. E. Bez, "A novel algorithm for initial lesion detection in ultrasound breast images," J. Appl. Clin. Med. Phys. **9**, 2741–■ (2008).

[40]M. Alemán-Flores, P. Alemán-Flores, R. Álvarez-León, R. Fuentes-Pavón, and J. M. Santana-Montesdeoca, "Computer vision techniques for breast tumor ultrasound analysis," Breast J. **14**, 483–486 (2008).

[41]N. R. S. Parveen, "Segmenting tumors in ultrasound images," International Conference on Computing Communication and Networking, 2008, pp. 1–5 (unpublished).

[42]B. Sahiner, H. P. Chan, M. A. Roubidoux, M. A. Helvie, L. M. Hadjiiski, A. Ramachandran, C. Paramagul, G. L. LeCarpentier, A. Nees, and C. Blane, "Computerized characterization of breast masses on three-dimensional ultrasound volumes," Med. Phys. **31**, 744–754 (2004).

[43]S. F. Huang, R. F. Chang, W. K. Moon, Y. H. Lee, D. R. Chen, and J. S. Suri, "Analysis of tumor vascularity using three-dimensional power Doppler ultrasound images," IEEE Trans. Med. Imaging **27**, 320–330 (2008).

[44]A. V. Alvarenga, W. C. A. Pereira, A. F. C. Infantosi, and C. M. Azevedo, "Complexity curve and grey level co-occurrence matrix in the texture evaluation of breast tumor on ultrasound images," Med. Phys. **34**, 379–387 (2007).

[45]J. Heinig, R. Witteler, R. Schmitz, L. Kiesel, and J. Steinhard, "Accuracy of classification of breast ultrasound findings based on criteria used for BI-RADS," Ultrasound Obstet. Gynecol. **32**, 573–578 (2008).

[46]H. W. Lee, B. D. Liu, K. C. Hung, S. F. Lei, P. C. Wang, and T. L. Yang, "Breast tumor classification of ultrasound images using wavelet-based channel energy and imageJ," IEEE J. Sel. Top. Signal Process. **3**, 81–93 (2009).

[47]M. L. Giger, "Computer-aided diagnosis of breast lesions in medical images," Comput. Sci. Eng. **2**, 39–45 (2000).

[48]J. P. Pluim, J. B. Maintz, and M. A. Viergever, "Mutual-information-based registration of medical images: A survey," IEEE Trans. Med. Imaging **22**, 986–1004 (2003). AQ: #9

[49]D. L. Hill, P. G. Batchelor, M. Holden, and D. J. Hawkes, "Medical image registration," Phys. Med. Biol. **46**, R1–R45 (2001).

AQ: #10